ISIJ International, Vol. 66 (2026), No. 12, pp. 1627–1637
https://doi.org/10.2355/isijinternational.ISIJINT-2026-179

Effect of Pressure on Steam/Supercritical Water Oxidation of 9Cr Steel and 18Cr Steel at 650°C

Yoshiaki TODA,[1)]* Nina KOBATA,[1)] Xianglan LI[2)] and Masahiko DEMURA[3)]

1) Center for Basic Research on Materials, National Institute for Materials Science, 1-2-1 Sengen, Tsukuba, Ibaraki 305-0047, Japan.
2) Advanced Engineering and Service Division, National Institute for Materials Science, 1-2-1 Sengen, Tsukuba, Ibaraki 305-0047, Japan.
3) Center for Basic Research on Materials, National Institute for Materials Science, 1-1 Namiki, Tsukuba, Ibaraki 305-0044, Japan.

(*Received June 24, 2026; Accepted September 7, 2026; Advance online published September 15, 2026; Published November 15, 2026*)

9Cr ferritic/martensitic steel and 18Cr austenitic steel were exposed to steam (0.5 MPa), subcritical water (10.2 MPa), and supercritical water (22.7 MPa) at 650°C for various durations. The pressure dependence of the oxidation rate constants of both steels was determined from the time dependence of specimen weight gain and oxide scale thickness due to oxidation. The oxidation rate constants of both steels decreased with increasing pressure. In steam, the oxidation rate constant of the 18Cr steel was smaller than that of the 9Cr steel. The difference in the oxidation rate constants between the two steels decreased with increasing pressure, and the oxidation rate constants became almost identical in supercritical water. The decrease in the oxidation rate constant with increasing pressure is considered to result from the reduction in voids in the formed oxide scales, which restricts the transport of metal and oxygen ions through the oxide scales.

KEY WORDS: heat-resistant steel; oxide scale; oxidation rate constant; oxidation reaction exponent; pressure; supercritical water.

1. Introduction

Understanding the steam oxidation behavior of heat-resistant materials is important for the safe long-term operation of boilers and pressure vessels. Therefore, many studies have been conducted on the oxidation behavior of heat-resistant metallic materials in high-temperature steam.[1,2)] In addition, recent high-efficiency thermal power plants generate supercritical water above 600°C and 25 MPa in boilers to drive power generation turbines.[3–6)] Furthermore, the use of supercritical water is also expected in light water reactors,[7,8)] and in geothermal power generation systems,[9,10)] which are effective for achieving carbon neutrality. Therefore, it is important to understand not only the oxidation of heat-resistant metallic materials in high-temperature steam but also their oxidation in supercritical water.

Many studies have investigated the oxidation behavior in supercritical water of 9Cr and 12Cr ferritic/martensitic steels and 18Cr austenitic steel, which have been widely used as boiler and pressure vessel materials in supercritical thermal power plants and are candidate cladding and structural materials for supercritical water reactors. The temperature dependence, dissolved oxygen dependence, and alloying/additional element dependence of the oxidation rate have been examined, and the structure and composition of oxide scales formed in supercritical water have been characterized.[7,8,11–21)] Recently, the supercritical water oxidation behavior of various heat-resistant metallic materials has also been analyzed and predicted using computational materials science.[22–25)] However, there have been very few systematic studies on the pressure dependence of oxidation behavior, such as comparisons between steam oxidation at atmospheric pressure and supercritical water oxidation under high pressure, or their relationship with subcritical water oxidation at intermediate pressures. For 9Cr and 12Cr ferritic/martensitic steels at 500–540°C, it has been reported that the oxidation rate in supercritical water at 25 MPa is higher than that in high-temperature steam at approximately 10 MPa.[16,17,21)] In contrast, there are also reports that the oxidation of 9Cr and 12Cr ferritic/martensitic steels becomes slower with increasing pressure.[18,26)]

In this study, to further investigate the effect of pressure on the oxidation behavior of heat-resistant steels, 9Cr ferritic/martensitic steel and 18Cr austenitic steel were exposed

* Corresponding author: E-mail: TODA.Yoshiaki@nims.go.jp

© 2026 The Iron and Steel Institute of Japan. This is an open access article under the terms of the Creative Commons Attribution-NonCommercial-NoDerivs license (https://creativecommons.org/licenses/by-nc-nd/4.0/).

for various durations at 650°C, which is close to the operating temperature of actual supercritical thermal power plants, to steam (0.5 MPa), subcritical water (10.2 MPa), and supercritical water (22.7 MPa) under different pressures. The time dependence of weight gain and oxide scale thickness due to oxidation was then measured. Based on these results, the pressure dependence of the oxidation rate constants of each specimen was evaluated. Observation and identification of the oxide scales were performed to investigate the effect of pressure on the oxidation behavior of heat-resistant steels at 650°C.

2. Experimental Procedure

In this study, a 9Cr-1Mo-V-Nb (mass%) ferritic/martensitic steel for boilers and pressure vessels (ASME SA-387/SA-387M Grade 91) and an 18Cr-8Ni (mass%) austenitic stainless steel (JIS G4304 SUS304) were investigated (hereafter referred to as 9Cr steel and 18Cr steel, respectively). The average compositions of the materials used are listed in **Table 1**.

Strip-shaped specimens with dimensions of 20 × 10 × 2 mm were cut from these commercial plates using electrical discharge machining. All surfaces of the specimens were mechanically polished with wet abrasive paper up to #600 grit to obtain approximately the same surface roughness for all specimens. The length, width, and thickness of each specimen were then measured with a precision of 1 μm to determine the total surface area. After cleaning and degreasing in an ultrasonic cleaner, each specimen was placed individually in an alumina crucible with a diameter of 26 mm and a depth of 19 mm, and dried at 150°C for 6 h using a drying oven. The specimens, including the crucibles, were then weighed using an electronic balance with a precision of 0.1 mg. Empty crucibles without specimens were also dried and weighed in order to measure the weight change of the crucibles themselves during the oxidation tests.

Figure 1 shows a schematic illustration of the steam/supercritical water oxidation test apparatus. In the pure water tank, the dissolved oxygen concentration in the pure water was reduced to less than 15 ppb by argon bubbling, and the electrical conductivity was reduced to less than 10 mS/m using ion-exchange resin. The crucibles containing the specimens and the empty crucibles were placed in a vertical cylindrical pressure vessel made of a nickel-based alloy with a volume of 2.8 L. The pressure vessel was heated using an electric furnace, and after the temperature inside the pressure vessel exceeded 200°C, pure water was supplied from the tank to the pressure vessel using a high-pressure pump. The pure water passed through a heat exchanger and a preheater from the tank, was gradually heated, and was supplied from the lower side of the pressure vessel. Steam discharged from the top of the pressure vessel was cooled through the heat exchanger and a cooler, and then returned to the pure water tank. In Fig. 1, the piping of the apparatus is shown in blue (low temperature), purple (medium temperature), and red (high temperature) according to the steam temperature in the pipes. When the inside of the pressure vessel was heated to 650°C, the pressure inside the vessel reached 0.5 MPa. Furthermore, by closing the back-pressure valve while operating the high-pressure pump, the pressure vessel was pressurized and filled with subcritical water (10.2 MPa) or supercritical water (22.7 MPa). The specimens and crucibles were

Table 1. Average compositions of the materials used (mass%).

	Fe	C	Si	Mn	Ni	Cr	Mo	V	Nb	Cu	N
9Cr steel	Bal.	0.10	0.24	0.44	0.04	8.74	0.94	0.21	0.076	–	0.058
18Cr steel	Bal.	0.043	0.45	0.90	8.09	18.36	0.15	–	0.018	0.24	0.053

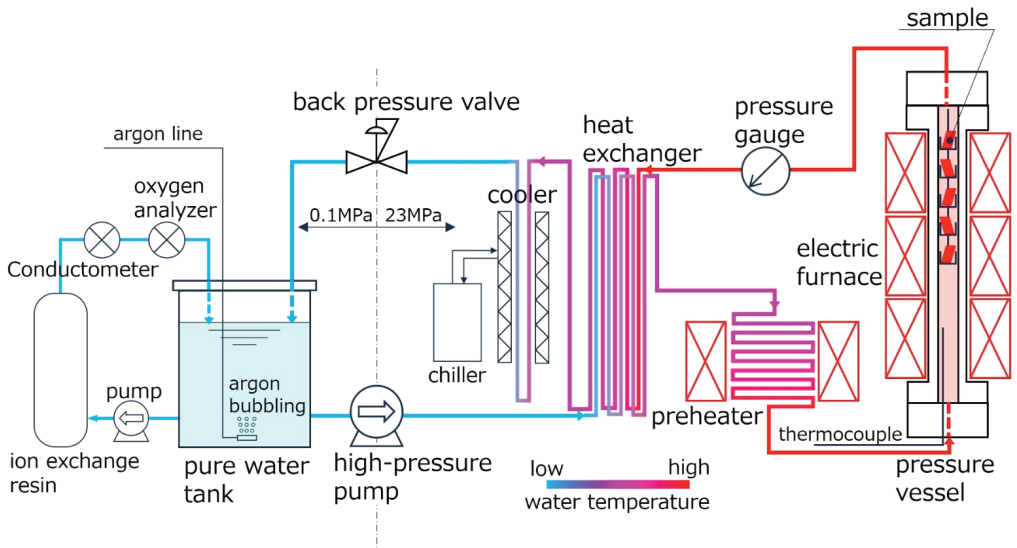

Fig. 1. Schematic illustration of the steam/supercritical water oxidation test apparatus. The piping of the apparatus is shown in blue (low temperature), purple (medium temperature), and red (high temperature) according to the steam/supercritical water temperature in the pipes.

© 2026 ISIJ

exposed to these environments for 0 h (in this case, only heating/pressurization and cooling/depressurization were performed), 20 h, 50 h, 72 h, and 195 h. After oxidation for a given period, the temperature inside the pressure vessel was decreased to 200°C and the pressure was reduced to atmospheric pressure. The steam inside the pressure vessel was then replaced with argon gas, and the vessel was cooled to room temperature.

Figure 2(a) shows the time dependence of the temperature and pressure inside the pressure vessel during the oxidation test at 650°C and 22.7 MPa for 50 h, indicated by the bold and narrow lines, respectively. Figure 2(b) shows the same changes in temperature and pressure inside the pressure vessel on the phase diagram of water. The solid curve near the center of Fig. 2(b) is the saturated vapor pressure curve, with the gas phase on the right side and the liquid phase on the left side. The region enclosed by the lines corresponding to temperatures above the critical temperature of 374.15°C and pressures above the critical pressure of 22.12 MPa in the upper right part of Fig. 2(b) is the supercritical water region. The heating/pressurization path is indicated by the solid circles, whereas the cooling/depressurization path is indicated by the open circles.

After the oxidation tests, the crucibles containing the specimens and the empty crucibles were removed from the pressure vessel and weighed using an electronic balance with a precision of 0.1 mg. The oxidation weight gain per unit area was calculated by dividing the weight difference before and after the test for each specimen including the crucible by the total surface area. The weight change of the crucibles was also taken into account in the weight change of the specimens.

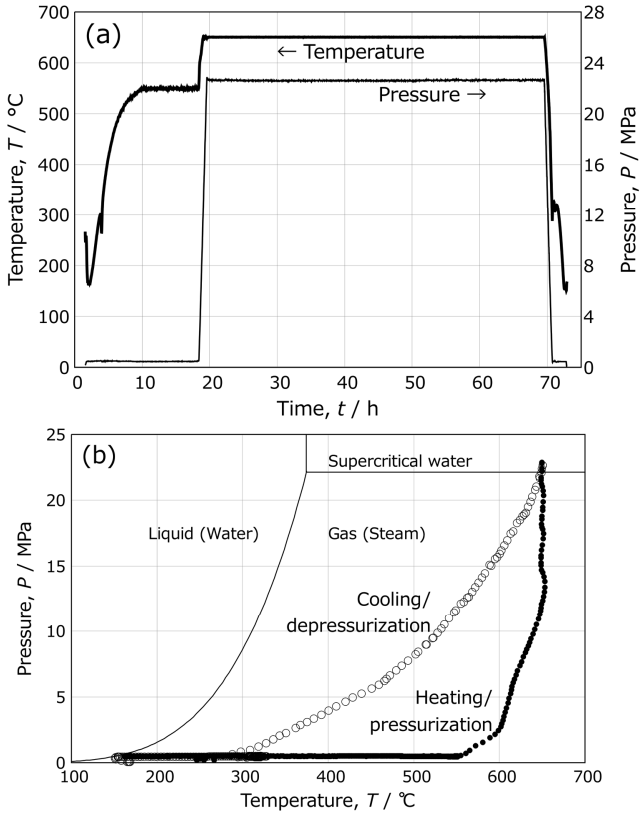

Fig. 2. (a) Time dependence of the temperature and pressure inside the pressure vessel during the oxidation test at 650°C and 22.7 MPa for 50 h, and (b) changes in temperature and pressure inside the pressure vessel shown on the phase diagram of water.

The oxidized specimens were embedded in an epoxy-based room-temperature-curing resin and sectioned using a low-load precision cutting machine. Cross sections of the oxide scales formed on the specimen surfaces were observed using secondary electron (SE) imaging with a scanning electron microscope (SEM, S-4700, Hitachi, Ltd.). The compositions of the oxide scales were analyzed using an energy-dispersive X-ray spectrometer (EDX, XFlash5030, Bruker) attached to the SEM, and the structures of them were analyzed using a Raman spectrometer (LabRAM HR, Horiba, Ltd.).

3. Experimental Results

3.1. Appearance of Oxidized Specimens

Figure 3 shows photographs of the 9Cr steel and 18Cr steel specimens kept in the crucibles after exposure to steam (0.5 MPa), subcritical water (10.2 MPa), and supercritical water (22.7 MPa) for 0 h (only heating/pressurization and cooling/depressurization), 20 h, 50 h, 72 h, and 195 h. The specimen dimensions were 20 mm in length and 10 mm in width. The 9Cr steel specimens oxidized in steam (0.5 MPa) remained silver-white, almost identical to the unoxidized state, up to 72 h. Partial spallation of the oxide scale was observed from 20 h, and large surface undulations were observed on the specimen surfaces after 72 h and 195 h. The 9Cr steel specimens oxidized in subcritical water (10.2 MPa) were brown from the initial stage of oxidation and became nearly black after 20 h. Partial spallation of the oxide scale occurred after 50 h, although the amount was smaller than that in the steam (0.5 MPa)-oxidized specimens. Surface undulations were observed on the specimen surface after oxidation for 195 h. The 9Cr steel specimens oxidized in supercritical water (22.7 MPa) exhibited a dark brown or dark gray appearance from the initial stage of oxidation. No spallation of the oxide scale was observed even after 195 h.

The 18Cr steel specimens oxidized in steam (0.5 MPa) changed in color from silver-white to gray and then to brown. Partial spallation of the oxide scale was observed from 20 h, and the amount appeared to be greater than that in the steam-oxidized 9Cr steel specimens. The color change of the 18Cr steel specimens oxidized in subcritical water (10.2 MPa) was similar to that of the subcritical-water-oxidized 9Cr steel specimens, whereas spallation of the surface scale was more pronounced than in the 9Cr steel. The 18Cr steel specimens oxidized in supercritical water (22.7 MPa) also exhibited the same color change as the 9Cr steel, and no spallation of the oxide scale was observed.

3.2. Time Dependence of Oxidation Weight Gain

Figure 4 shows the oxidation weight gain per unit area as a function of oxidation time at 650°C in steam (0.5 MPa), subcritical water (10.2 MPa), and supercritical water (22.7 MPa) for (a) 9Cr steel and (b) 18Cr steel, indicated by filled/open triangles, squares, and circles, respectively. In the time-series data obtained from the same sample under the same test condition, data points showing values smaller than the surrounding trend are indicated by open

© 2026 ISIJ

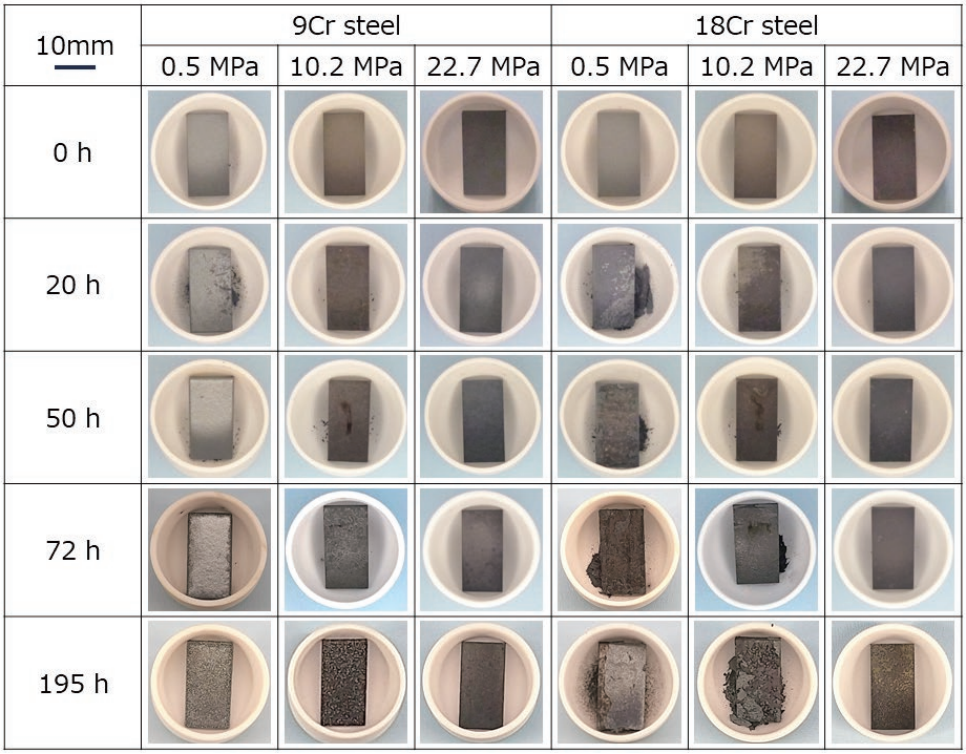

Fig. 3. Appearance photographs of the 9Cr steel and 18Cr steel specimens after exposure at 650°C to steam (0.5 MPa), subcritical water (10.2 MPa), and supercritical water (22.7 MPa) for 0 h (only heating/pressurization and cooling/depressurization), 20 h, 50 h, 72 h, and 195 h.

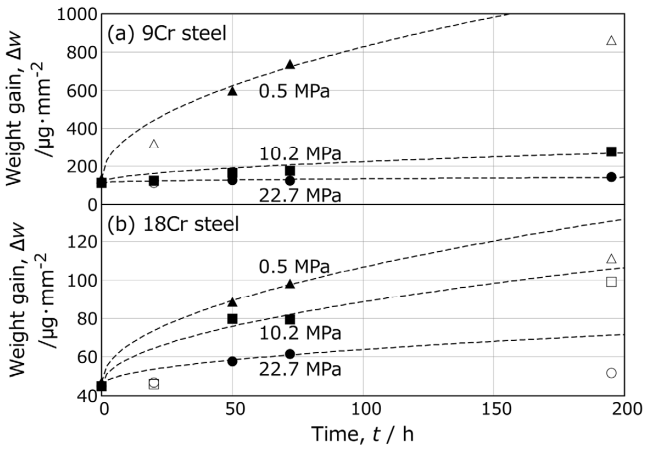

Fig. 4. Oxidation weight gain per unit area as a function of oxidation time at 650°C in steam (0.5 MPa), subcritical water (10.2 MPa), and supercritical water (22.7 MPa), and their regression curves for (a) 9Cr steel and (b) 18Cr steel.

symbols. For these samples, the spalled oxide scale may not have remained in the crucible, and the oxidation weight gain may therefore not have been measured accurately. Since these data are suspected to underestimate the weight gain, only the data indicated by filled symbols were used for the analysis of the time dependence described below. The specimens also oxidized and gained weight during the heating/pressurization process before the oxidation tests, and cooling/depressurization process after the tests. Therefore, it should be noted that the oxidation weight gain was not 0 μg/mm^2 even when the oxidation time at the target temperature and pressure was 0 h.

At all pressures, the oxidation weight gain of the 9Cr steel was larger than that of the 18Cr steel. Note that the scales of the vertical axes are different between (a) 9Cr steel and (b) 18Cr steel. For both steels, the oxidation weight gain was the largest in steam (0.5 MPa), followed by subcritical water (10.2 MPa) and supercritical water (22.7 MPa), in which the oxidation weight gain decreased in this order.

Table 2. Oxidation reaction exponent, n determined from oxidation weight gain, and oxidation rate constant, k_w determined assuming $n = 2$.

Sample	P [MPa]	n	k_w [μg^{2}mm^{-4}h^{-1}] (assume $n = 2$)
9Cr steel	0.5	1.68	4 827.01
	10.2	2.33	124.84
	22.7	1.67	3.87
18Cr steel	0.5	1.73	35.95
	10.2	2.19	19.03
	22.7	1.56	3.44

The time, t dependence of the oxidation weight gain, Δw is often described by the following equation.[12,14–17,19–21,26]

$$\left(\Delta w - \Delta w_0\right)^n = k_w t \quad \text{..... (1)}$$

Here, Δw_0 is the oxidation weight gain at an oxidation time of 0 h, n is the oxidation reaction exponent, and k_w is the oxidation rate constant determined from the oxidation weight gain. By rearranging Eq. (1),

$$n \log\left(\Delta w - \Delta w_0\right) = \log k_w + \log t \quad \text{..... (2)}$$

is obtained. Therefore, the slopes, n were determined by linear regression of the double-logarithmic plots of the experimental data for oxidation weight gain, $(\Delta w - \Delta w_0)$ and time, t shown in Fig. 4, and the results are listed in **Table 2**.

© 2026 ISIJ

Under the steel grades and pressure conditions investigated in this study, n ranged from 1.5 to 2.3. The variation in the n values is considered to result from measurement errors in the oxidation weight gain due to oxide scale spallation and other factors, as well as measurement errors in the oxidation weight gain Δw_0 at an oxidation time of 0 h.

As shown in Fig. 4, at all pressures, the change in oxidation weight gain of both steels clearly decreased with increasing oxidation time. This indicates that, at all pressures investigated in this study, the oxidation process was rate-controlled by mass transport through the oxide scales. Therefore, it is reasonable to consider that the steam and supercritical water oxidation observed in this study followed the parabolic rate law with $n = 2$. In addition, previous studies have analyzed the oxidation weight gain of metallic materials in supercritical water using the parabolic rate law with $n = 2$, as in the case of oxidation in steam at atmospheric pressure.[12,15,17,19,26] Table 2 also lists the oxidation rate constant, k_w obtained by linear regression assuming $n = 2$. The dashed curves in Fig. 4 represent the parabolic curves of Eq. (1) drawn using the obtained k_w with the assumption of $n = 2$. It can be seen that the weight gain due to oxidation can be described by Eq. (1).

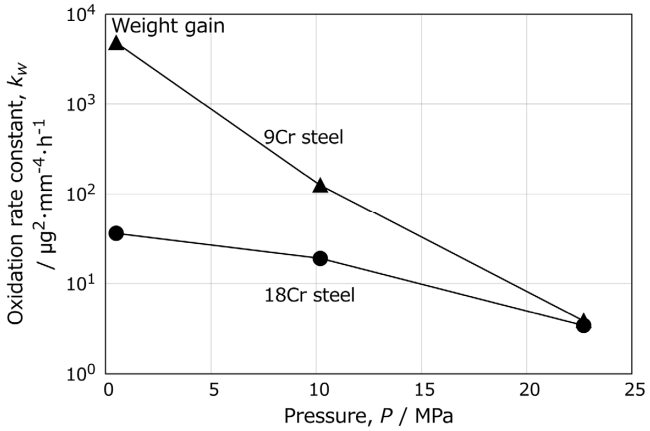

Fig. 5. Pressure dependence of the oxidation rate constants determined from the oxidation weight gain of the 9Cr steel and 18Cr steel at 650°C.

Figure 5 shows the pressure dependence of the oxidation rate constants of the 9Cr steel and 18Cr steel, indicated by the triangles and circles, respectively. The oxidation rate constants of both the 9Cr steel and the 18Cr steel decreased monotonically with increasing pressure. The degree of decrease was greater for the 9Cr steel than for the 18Cr steel. Notably, in supercritical water (22.7 MPa), the oxidation rate constants of the 9Cr steel and the 18Cr steel converged to nearly the same value. Thus, oxidation was significantly suppressed in supercritical water, and the difference between the two alloys disappeared.

3.3. Cross-sectional Microstructures of Oxide Scales

Figure 6 shows SEM secondary electron images of cross sections of oxide scales formed on the 9Cr steel after exposure to steam (0.5 MPa), subcritical water (10.2 MPa), and supercritical water (22.7 MPa) at 650°C for 20 h, 50 h, and 195 h, respectively. The SEM images of the oxide scales formed in steam (0.5 MPa) are shown at a different magnification from those formed at the other pressures. In each image, the boundary between the black and gray regions in the upper part corresponds to the specimen surface, and the light gray region in the lower part corresponds to the

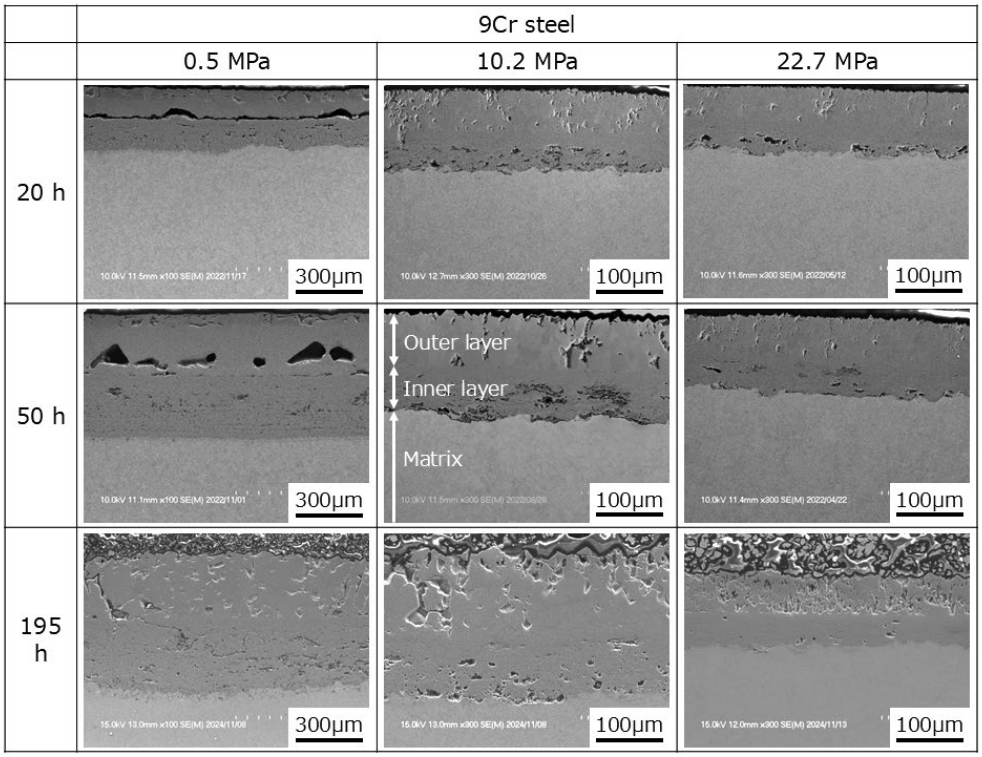

Fig. 6. SEM secondary electron images of cross sections of oxide scales formed on the 9Cr steel after exposure to steam (0.5 MPa), subcritical water (10.2 MPa), and supercritical water (22.7 MPa) at 650°C for 20 h, 50 h, and 195 h, respectively. The outer layer, inner layer, and metallic substrate are indicated by white arrows, respectively, on the left side of the center SEM image.

© 2026 ISIJ

metallic substrate. The region between them, where dark gray contrast and voids are observed, corresponds to the oxide scale, in which outer and inner layers were observed. In one of the SEM images in Fig. 6, the outer layer, inner layer, and metallic substrate are indicated by white arrows, on the left side of the image.

The oxide scale thickness of the 9Cr steel increased with oxidation time from approximately 300 μm to approximately 900 μm in steam (0.5 MPa), and from approximately 100 μm to approximately 200 μm in subcritical water (10.2 MPa). In supercritical water (22.7 MPa), no clear growth of the oxide scale was observed, and the oxide scale thickness remained approximately 100 μm at all exposure times. Voids were observed in the oxide scales formed on the 9Cr steel in steam (0.5 MPa), particularly in the middle region along the thickness direction. After 20 h, the voids became horizontally continuous, resembling cracks. After 50 h, the thickness of the void regions increased, while their continuity disappeared. The size of the voids located above the central region of the oxide scale exceeded 100 μm. After 195 h, the size of the voids decreased, although voids were observed throughout the entire oxide scale. In contrast, the oxide scales formed in subcritical water (10.2 MPa) and supercritical water (22.7 MPa) clearly contained fewer and smaller voids.

Figure 7 shows the results of EDX compositional analysis of cross sections of oxide scales formed on the 9Cr steel after exposure to (a) steam (0.5 MPa) and (b) supercritical water (22.7 MPa) for 50 h. Secondary electron (SE) images and elemental mappings of iron, chromium, molybdenum, and oxygen are presented together. In the oxygen mappings, the colored regions correspond to the oxide scale, with the free surface on the upper side and the metallic substrate on the lower side. Although the oxide scales appeared to have nearly uniform contrast in the SE images, the elemental mappings revealed that the oxide scales consisted of two layers, namely an outer layer and an inner layer. The outer layer contained no chromium and consisted of iron oxide containing a lower concentration of molybdenum than the base steel. The inner layer consisted of iron oxide containing a higher concentration of chromium than the base steel and nearly the same concentration of molybdenum as the base steel. In the oxide scales formed in (a) steam (0.5 MPa) and (b) supercritical water (22.7 MPa) shown in Fig. 7, the elemental concentration were almost the same in both the outer and inner layers. The voids observed in the oxide scale formed in steam (0.5 MPa) were predominantly formed on the outer-layer side along the boundary between the inner and outer layers.

Figure 7(c) shows the results of Raman spectroscopic analysis of the inner layer of the oxide scale formed in supercritical water (22.7 MPa). Analysis of two other locations in the inner layer of the oxide scale also revealed peaks at wavenumbers of 313–322 cm^{-1}, 541–549 cm^{-1}, and 669–680 cm^{-1}, which were identified as magnetite-type iron oxide.[27,28] Similarly, peaks at wavenumbers of 297–319 cm^{-1}, 542–546 cm^{-1}, and 666–669 cm^{-1} were obtained from the outer layer of the oxide scale, and were also identified as magnetite-type iron oxide.[27,28] Similar Raman spectra were obtained from both the inner and outer layers of the oxide scales formed in steam (0.5 MPa), and these were likewise identified as magnetite-type iron oxide. Combined with the elemental mapping results, it is considered that the outer layer consisted of chromium-free magnetite-type iron oxide, Fe_3O_4, whereas the inner layer consisted of magnetite-type iron oxide, $(Fe, Cr)_3O_4$, in which chromium partially substituted for iron. The types and structures of the oxides formed on the 9Cr steel were

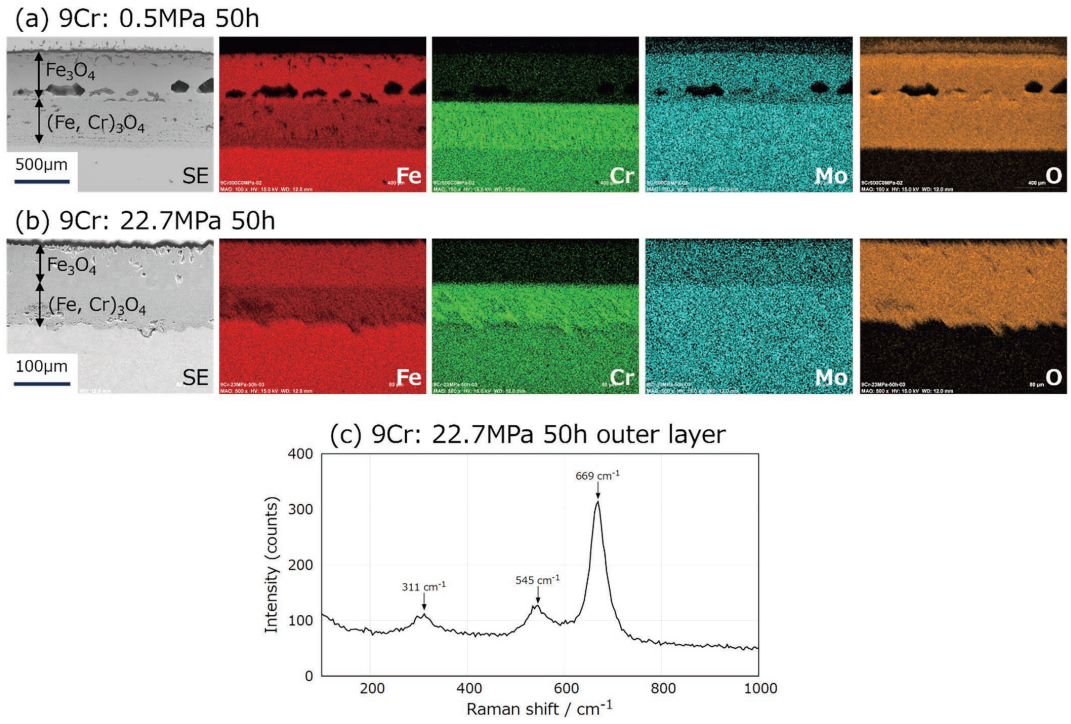

Fig. 7. Secondary electron (SE) images and elemental mappings of cross sections of oxide scales formed on the 9Cr steel after exposure to (a) steam (0.5 MPa) and (b) supercritical water (22.7 MPa) for 50 h, and (c) Raman spectroscopic profile obtained from the oxide scale formed in supercritical water.

© 2026 ISIJ

the same as those observed in previous studies on steam oxidation and supercritical water oxidation.[7,8,11,13,16,17)]

Figure 8 shows SEM secondary electron images of cross sections of oxide scales formed on the 18Cr steel after exposure to steam (0.5 MPa), subcritical water (10.2 MPa), and supercritical water (22.7 MPa) at 650°C for 20 h, 50 h, and 195 h, respectively. The interpretation of the images is the same as that for the 9Cr steel shown in Fig. 6. The time dependence of the oxide scale thickness of the 18Cr steel was smaller than that of the 9Cr steel. The oxide scale thickness increased from approximately 70 μm to approximately 100 μm in steam (0.5 MPa), and from approximately 50 μm to approximately 80 μm in subcritical water (10.2 MPa) and supercritical water (22.7 MPa). Under all conditions, the oxide scales were divided into inner and outer layers.

Voids were observed in the oxide scales formed on the 18Cr steel in steam (0.5 MPa), particularly in the outer layer and between the inner and outer layers. These voids increased in size with increasing exposure time. In subcritical water (10.2 MPa), the voids in the oxide scale became larger after 50 h, whereas in supercritical water (22.7 MPa), they became larger after 20 h; however, the voids subsequently became smaller again with increasing exposure time. In addition, the number of voids decreased and their size became smaller with increasing pressure.

Figure 9 shows the results of EDX compositional analysis of cross sections of oxide scales formed on the 18Cr steel after exposure to (a) steam (0.5 MPa) and (b) supercritical water (22.7 MPa) for 50 h, and the interpretation of the figure is the same as that for the 9Cr steel in Fig. 7. The outer layer consisted of iron oxide composed of iron and oxygen, whereas the inner layer consisted of iron oxide containing a higher concentration of chromium than the base steel and nearly the same concentration of nickel as the base steel. The elemental concentrations were almost the same in the oxide scales formed in both (a) steam (0.5 MPa) and (b) supercritical water (22.7 MPa). In both cases, the voids were distributed within the outer layer.

The results of Raman spectroscopic analysis of the outer and inner layers of the oxide scale formed in supercritical water (22.7 MPa) are shown in Figs. 9(c) and 9(d), respectively. Including two additional locations other than those shown in Fig. 9(c), peaks were obtained from the outer layer at wavenumbers of 300–319 cm^{-1}, 542–546 cm^{-1}, and 666–669 cm^{-1}. Therefore, the outer layer was identified as magnetite-type iron oxide.[27,28)] Including two additional locations other than those shown in Fig. 9(d), peaks were obtained from the inner layer at wavenumbers of 599 cm^{-1} and 680 cm^{-1}, and the inner layer was therefore identified as spinel-type iron oxide.[29,30)] Combined with the elemental mapping results, it is considered that the outer layer consisted of Fe_3O_4, whereas the inner layer consisted of $FeCr_2O_4$ partially substituted by nickel. These oxides formed on the 18Cr steel were consistent with those reported in previous studies.[7,20)]

3.4. Pressure Dependence of Oxide Scale Thickness Change

Figure 10 shows the change in oxide scale thickness with oxidation time in steam (0.5 MPa), subcritical water (10.2 MPa), and supercritical water (22.7 MPa) for (a) 9Cr steel and (b) 18Cr steel, indicated by filled/open triangles, squares, and circles, respectively. Similar to the oxidation weight gain plots in Fig. 4, the open symbols indicate data

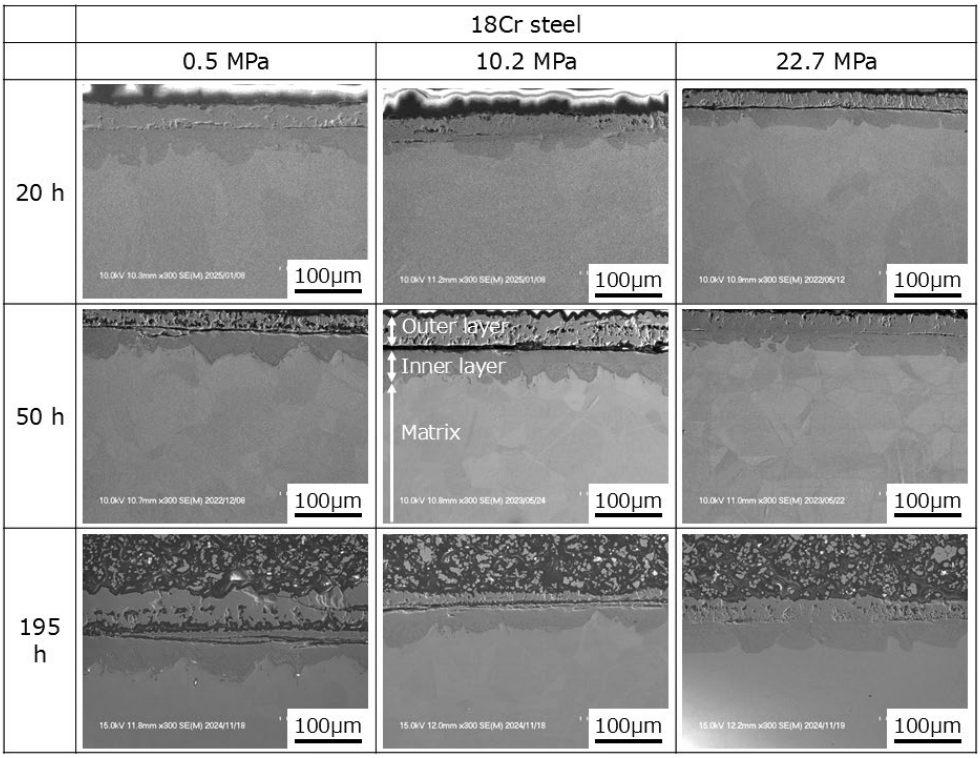

Fig. 8. SEM secondary electron images of cross sections of oxide scales formed on the 18Cr steel after exposure to steam (0.5 MPa), subcritical water (10.2 MPa), and supercritical water (22.7 MPa) at 650°C for 20 h, 50 h, and 195 h, respectively. The outer layer, inner layer, and metallic substrate are indicated by white arrows, respectively, on the left side of the center SEM image.

© 2026 ISIJ

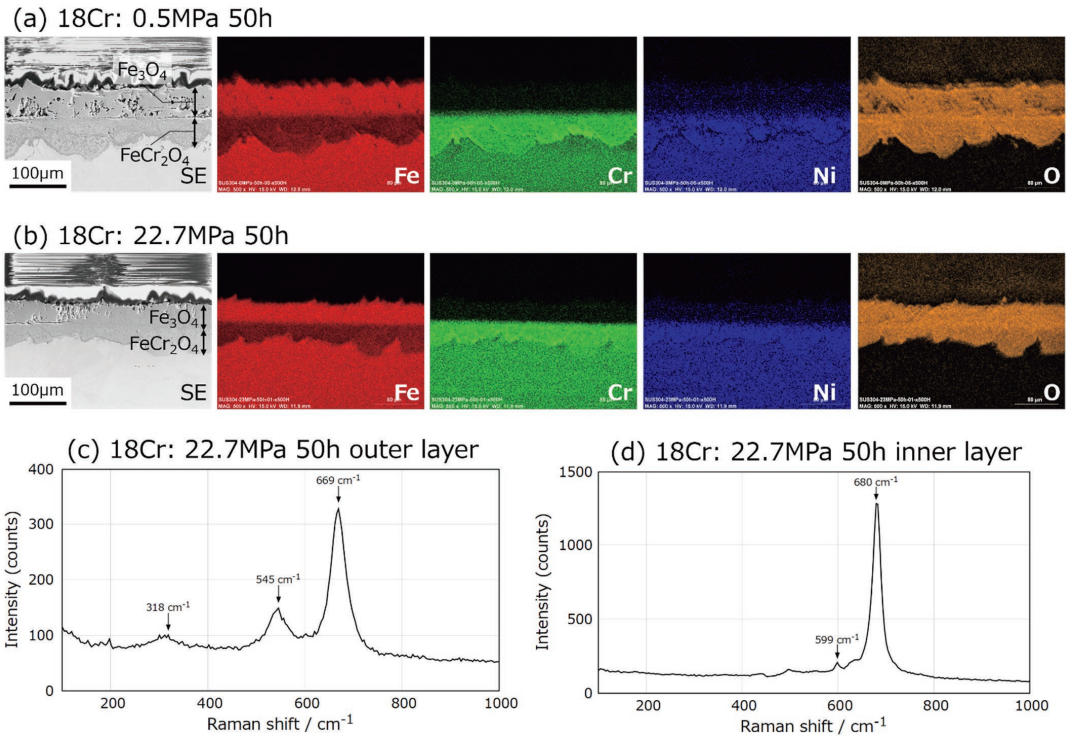

Fig. 9. Secondary electron (SE) images and elemental mappings of cross sections of oxide scales formed on the 18Cr steel after exposure to (a) steam (0.5 MPa) and (b) supercritical water (22.7 MPa) for 50 h, and Raman spectroscopic profiles obtained from the (c) outer layer and (d) inner layer of the oxide scale formed in supercritical water.

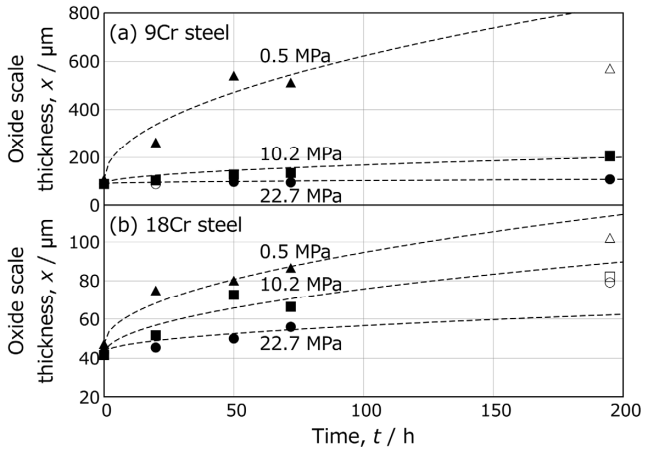

Fig. 10. Changes in oxide scale thickness with oxidation time at 650°C in steam (0.5 MPa), subcritical water (10.2 MPa), and supercritical water (22.7 MPa), and their regression curves for (a) 9Cr steel and (b) 18Cr steel.

Table 3. Oxidation reaction exponent, n determined from oxide scale thickness, and oxidation rate constant, k_x determined assuming $n = 2$.

Sample	P [MPa]	n	k_x [$\mu m^2 h^{-1}$] (assume $n = 2$)
9Cr steel	0.5	2.22	2 666.66
	10.2	1.96	62.15
	22.7	2.17	1.70
18Cr steel	0.5	2.34	22.65
	10.2	2.08	11.55
	22.7	1.24	1.95

suspected to be underestimated based on the surrounding trend, and these data were excluded from the analysis described below. Since oxide scales were also formed during the heating/pressurization process before the oxidation tests, and cooling/depressurization process after the tests, the oxide scale thickness was not 0 μm even when the oxidation time was 0 h. The oxide scale thickness of the 9Cr steel was larger than that of the 18Cr steel at all pressures. For both steels, the oxide scale thickness was the largest in steam (0.5 MPa), followed by subcritical water (10.2 MPa) and supercritical water (22.7 MPa), in which the thickness decreased in this order.

The time, t dependence of the oxide scale thickness, x was also assumed to follow Eq. (3), similarly to Eq. (1).[12,15,17,19,26]

$$(x - x_0)^n = k_x t \quad \text{..... (3)}$$

Here, x_0 is the oxide scale thickness at an oxidation time of 0 h, and k_x is the oxidation rate constant determined from the oxide scale thickness. As described in Section 3.2, the slopes, n were determined by linear regression of the double-logarithmic plots of the oxide scale thickness, $(x - x_0)$ and time, t shown in Fig. 10, and the results are listed in **Table 3**. In the case of the 18Cr steel in supercritical water (22.7 MPa), $n = 1.24$, which was a relatively low value, whereas under the other steel grades and pressure conditions, n was approximately 2. Therefore, the k_x was calculated from the experimental data of $(x - x_0)$ and t assuming $n = 2$, and the results are listed in Table 3. The interpretation of the variation in the n values obtained from the experimental data in Table 3 and the validity of assuming $n = 2$ are the same as those described in Section 3.2. The dashed curves in Fig. 10 represent the parabolic curves

© 2026 ISIJ

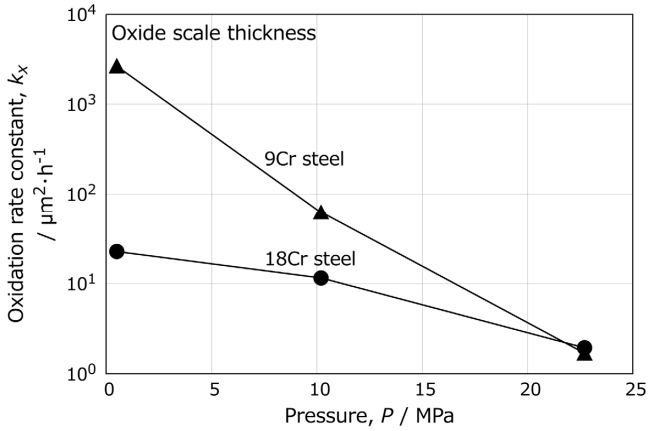

Fig. 11. Pressure dependence of the oxidation rate constants determined from the oxide scale thicknesses of the 9Cr steel and 18Cr steel at 650°C.

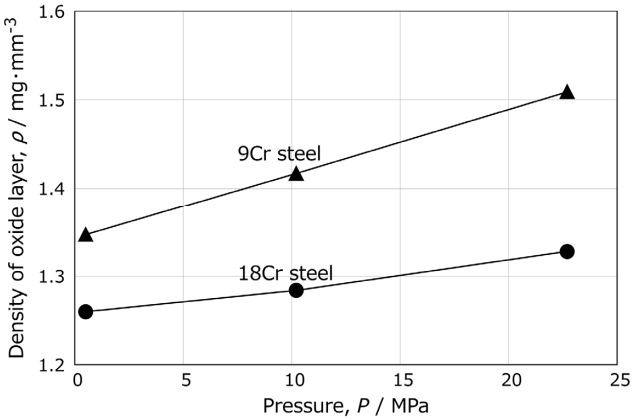

Fig. 12. Pressure dependence of the oxide scale densities of the 9Cr steel and 18Cr steel at 650°C.

of Eq. (3) drawn under the condition of $n = 2$ using the obtained k_x. The time dependence of the oxide scale thickness is well described by Eq. (3).

Figure 11 shows the pressure dependence of the oxidation rate constants determined from the oxide scale thicknesses of the 9Cr steel and 18Cr steel, indicated by the triangles and circles, respectively. Results similar to the pressure dependence of the oxidation rate constants determined from the oxidation weight gain shown in Fig. 5 were obtained. The oxidation rate constants of both the 9Cr steel and the 18Cr steel decreased monotonically with increasing pressure. The degree of decrease was greater for the 9Cr steel than for the 18Cr steel. As in the case of the oxidation weight gain, the oxidation rate constants of the 9Cr steel and the 18Cr steel became almost identical in supercritical water (22.7 MPa).

4. Discussion

4.1. Voids in Oxide Scales

The pressure dependence of the oxidation rate constants at 650°C for 9Cr ferritic heat-resistant steel and 18Cr austenitic steel, which are used as heat-resistant steels for boilers and pressure vessels, was evaluated from the weight change of the specimens (Fig. 4) and the change in oxide scale thickness (Fig. 10). As a result, the oxidation rate constants of both steels decreased with increasing pressure (Figs. 5 and 11). This suggests that, at 650°C, which is close to the actual operating temperature of supercritical thermal power plants, boilers and pressure vessels can be safely operated using higher-pressure subcritical water or supercritical water at the same temperature if they are designed based on the oxidation behavior of heat-resistant steels in steam at atmospheric pressure.

At both steam and supercritical water pressures, the oxides formed on the 9Cr steel were of the same type and structure, showing no pressure dependence (Fig. 7). In addition, the types of oxides formed on the 18Cr steel also showed no pressure dependence. In other words, the decrease in the oxidation rate constants with increasing pressure was not caused by differences in the oxide types.

Several voids were observed in the oxide scales formed on the 9Cr steel in steam (0.5 MPa). In particular, large voids were observed in the outer-layer Fe_3O_4, in which chromium was not substituted. However, in the oxide scales formed in subcritical water (10.2 MPa) and supercritical water (22.7 MPa), the voids became smaller and less numerous (Figs. 6 and 7). In the 18Cr steel as well, the number of voids in the oxide scales decreased with increasing pressure (Figs. 8 and 9). These differences in the amount and size of the voids are considered to be related to the decrease in the oxidation rate.

The apparent density, ρ of the oxide scale can be calculated by dividing the oxidation rate constant determined from the oxidation weight gain, k_w (Fig. 5) by the oxidation rate constant determined from the oxide scale thickness, k_x (Fig. 11). **Figure 12** shows the pressure dependence of the oxide scale density of the 9Cr steel and 18Cr steel formed under the three pressure conditions indicated by the triangles and circles, respectively. The oxide scale densities formed on the 9Cr steel in steam (0.5 MPa) and supercritical water (22.7 MPa) were 1.35 mg/mm^3 and 1.51 mg/mm^3, respectively. In previous studies, the oxide scale densities of 9Cr steel (NF616) and 12Cr steel (HCM12A) were evaluated as 1.58 mg/mm^3[11] and 1.37 mg/mm^3,[13] respectively. Therefore, the oxide scale density values shown in Fig. 12 are considered reasonable. In addition, the oxide scale densities formed on the 18Cr steel in steam (0.5 MPa) and supercritical water (22.7 MPa) were 1.26 mg/mm^3 and 1.33 mg/mm^3, respectively. The oxide scale densities of both the 9Cr steel and the 18Cr steel increased monotonically with increasing pressure. This increase in oxide scale density corresponds to a decrease in the volume of voids in the oxide scales. The decrease in the time dependence of the oxidation weight gain (Fig. 4) and oxide scale thickness (Fig. 10) of the 9Cr steel and 18Cr steel with increasing pressure, resulting in a monotonic decrease in the oxidation rate constants (Figs. 5 and 11), is considered to be closely related to the monotonic decrease in the volume of voids in the oxide scales (Fig. 12).

During steam (0.5 MPa) oxidation, steam gas is considered to directly penetrate into macroscopic voids in the oxide scales, allowing oxidation to proceed through mass transport faster than bulk diffusion through the oxide scales. With increasing pressure, the volume of voids in the oxide scales decreases, which is expected to suppress the mass transport due to direct penetration of steam gas and thereby decrease the oxidation rate.

© 2026 ISIJ

In the 9Cr steel, magnetite-type iron oxides, Fe_3O_4 and $(Fe, Cr)_3O_4$, were formed. In the 18Cr steel, magnetite-type iron oxide was formed in the outer layer, whereas $FeCr_2O_4$ spinel-type complex oxide was formed in the inner layer. Since the diffusion of elements and ions is slower in the spinel-type complex oxide than in the magnetite-type iron oxide, the former has a greater effect in suppressing oxidation. Therefore, in steam (0.5 MPa), the oxidation rate constant of the 18Cr steel was smaller than that of the 9Cr steel.

As described above, with increasing pressure, the void volume in the oxide scales, particularly in the magnetite-type iron oxide, decreased, thereby suppressing oxidation. Moreover, as shown in Fig. 12, the decrease in the void volume in the oxide scales was greater for the 9Cr steel than for the 18Cr steel. Therefore, with increasing pressure, the oxidation rate constant of the 9Cr steel decreased more markedly than that of the 18Cr steel. Under supercritical water (22.7 MPa) conditions, the effect of oxidation suppression caused by the reduced void volume in the oxide scales is considered to have become comparable to the protective effect of the spinel-type complex oxide, resulting in similar oxidation rate constants for the 9Cr steel and 18Cr steel. Reducing the volume of macroscopic defects in the oxide scale may enable even an iron-dominant oxide to act as a protective oxide scale.

4.2. Comparison with Previous Studies

To the best of the authors' knowledge, no previous studies focusing on the pressure dependence of steam/supercritical water oxidation of 9Cr ferritic/martensitic steel or 18Cr austenitic steel have been reported. Previous studies that investigated oxidation behavior under different pressures within a single paper are summarized in **Table 4**. The table lists the test conditions that are considered to affect the oxidation behavior, including chromium content, temperature, pressure, oxidation time, and dissolved oxygen concentration. The type of experimental apparatus (batch-type or flow-type) is also included as one of the test conditions. Some previous studies on supercritical water oxidation employed batch-type experiments using sealed autoclaves.[21,26] However, it has been pointed out that even under the same supercritical water conditions, the oxidation environment differs from that in flow-type oxidation test apparatuses, resulting in differences in oxidation behavior.[2] On the right side of Table 4, the effects of increasing pressure on oxidation are categorized as either "accelerated", "suppressed", or "independent".

In this study, the time dependence of oxidation weight gain and oxide scale thickness of the 9Cr ferritic/martensitic steel at three different pressures at 650°C was investigated using the same experimental apparatus. As a result, increasing the pressure of steam/supercritical water suppressed the oxidation of the 9Cr steel. In addition, previous studies have also reported that increasing the pressure of steam/supercritical water suppresses oxidation at high temperatures above 600°C.[26] No previous studies investigating the pressure dependence of void morphology in oxide scales were found. However, for ferritic/martensitic steels at high temperatures above 600°C, the reduction in voids with increasing pressure may suppress oxidation. In contrast, at temperatures below 600°C, both results showing that increasing the pressure of steam/supercritical water accelerates oxidation[16,17,21] and results showing that it suppresses oxidation[18] have been reported. No clear relationship between the pressure dependence of oxidation and the test conditions could be identified from Table 4. At temperatures below 600°C, mechanisms other than the reduction in voids are likely to affect oxidation.

For the 18Cr austenitic steel, Table 4 indicates that increasing the pressure of steam/supercritical water suppresses oxidation over a wide temperature range. No previous studies investigating the pressure dependence of oxide scale morphology in 18Cr austenitic steel were found. However, it is considered that the reduction in voids with increasing pressure suppresses oxidation over a wide temperature range.

5. Conclusions

9Cr ferritic/martensitic heat-resistant steel and 18Cr aus-

Table 4. Previous studies investigating steam/supercritical water oxidation of 9Cr ferritic/martensitic steel and 18Cr austenitic steel under different pressures.

Alloy	Cr content (mass%)	Temp. [°C]	Pressure [MPa]	Oxidation duration [h]	Dissolved Oxygen content [ppb]	Experimental device type	Effect of increasing pressure on oxide	References
T91	8.90	400 500	25 and 30	780	8 000	Flow	Independent Suppressed	18)
NF616	8.82	500	10.8 and 25	2 000	10	Flow	Accelerated	16, 17)
T91	8.91	540	9.9 and 25	120	40	Batch	Accelerated	21)
Grade 91	8.74	650	0.5 and 10.2 and 22.7	195	15	Flow	Suppressed	This work
NF616	9.02	600 700	1 and 10	250 350	7	Batch	Suppressed Independent	26)
HCM12A	10.83	500	10.8 and 25	2 000	10	Flow	Accelerated	16, 17)
HCM12A	10.78	600 700	1 and 10	250 350	7	Batch	Suppressed Independent	26)
316L	16.68	400 and 500	25 and 30	780	8 000	Flow	Suppressed	18)
SUS304	18.36	650	0.5 and 10.2 and 22.7	195	15	Flow	Suppressed	This work

© 2026 ISIJ

tenitic steel were exposed for various durations in a pressure vessel to steam (0.5 MPa), subcritical water (10.2 MPa), and supercritical water (22.7 MPa) at 650°C. The pressure dependence of the oxidation rate constants of each material was determined from the time dependence of specimen weight gain and oxide scale thickness due to oxidation. The oxidation rate constants of both steels decreased with increasing pressure. In steam, the oxidation rate constant of the 18Cr steel was smaller than that of the 9Cr steel. The difference between the two steels decreased with increasing pressure, and the oxidation rate constants of the two steels became almost identical in supercritical water. These results suggest that, at 650°C, boilers and pressure vessels can be safely operated using higher-pressure steam or supercritical water at the same temperature if they are designed based on the oxidation behavior of heat-resistant steels in steam at atmospheric pressure. The decrease in the oxidation rate constants with increasing pressure is considered to result from the reduction in voids in the formed oxide scales, which is expected to suppress the mass transport due to direct penetration of steam gas.

Statement for Conflict of Interest

The authors declare no conflicts of interest regarding this manuscript.

Acknowledgments

This study was supported by JSPS KAKENHI Grant Number 25K08550 and the 35th ISIJ Research Promotion Grant from the Iron and Steel Institute of Japan.

REFERENCES

1) S. R. J. Saunders, M. Monteiro and F. Rizzo: *Prog. Mater Sci.*, **53** (2008), 775. https://doi.org/10.1016/j.pmatsci.2007.11.001
2) I. G. Wright and R. B. Dooley: *Int. Mater. Rev.*, **55** (2010), 129. https://doi.org/10.1179/095066010X12646898728165
3) F. Masuyama: *ISIJ Int.*, **41** (2001), 612. https://doi.org/10.2355/isijinternational.41.612
4) T.-U. Kern, M. Staubli and B. Scarlin: *ISIJ Int.*, **42** (2002), 1515. https://doi.org/10.2355/isijinternational.42.1515
5) R. Viswanathan, J. F. Henry, J. Tanzosh, G. Stanko, J. Shingledecker, B. Vitalis and R. Purgert: *J. Mater. Eng. Perform.*, **14** (2005), 281. https://doi.org/10.1361/10599490524039
6) F. Abe: *Engineering*, **1** (2015), 211. https://doi.org/10.15302/j-eng-2015031
7) G. S. Was, P. Ampornrat, G. Gupta, S. Teysseyre, E. A. West, T. R. Allen, K. Sridharan, L. Tan, Y. Chen, X. Ren and C. Pister: *J. Nucl. Mater.*, **371** (2007), 176. https://doi.org/10.1016/j.jnucmat.2007.05.017
8) C. Sun, R. Hui, W. Qu and S. Yick: *Corros. Sci.*, **51** (2009), 2508. https://doi.org/10.1016/j.corsci.2009.07.007
9) M. Hermanská, A. Stefánsson and S. Scott: *Geothermics*, **78** (2019), 101. https://doi.org/10.1016/j.geothermics.2018.11.002
10) Y. Yamaya: *Surveys in Geophysics*, **47** (2026), 595. https://doi.org/10.1007/s10712-025-09907-6
11) Y. Chen, K. Sridharan, T. Allen and S. Ukai: *J. Nucl. Mater.*, **359** (2006), 50. https://doi.org/10.1016/j.jnucmat.2006.07.021
12) Y. Chen, K. Sridharan and T. Allen: *Corros. Sci.*, **48** (2006), 2843. https://doi.org/10.1016/j.corsci.2005.08.021
13) L. Tan, M. T. Machut, K. Sridharan and T. R. Allen: *J. Nucl. Mater.*, **371** (2007), 161. https://doi.org/10.1016/j.jnucmat.2007.05.001
14) P. Ampornrat and G. S. Was: *J. Nucl. Mater.*, **371** (2007), 1. https://doi.org/10.1016/j.jnucmat.2007.05.023
15) L. Tan, X. Ren and T. R. Allen: *Corros. Sci.*, **52** (2010), 1520. https://doi.org/10.1016/j.corsci.2009.12.032
16) J. Bischoff and A. T. Motta: *J. Nucl. Mater.*, **424** (2012), 261. https://doi.org/10.1016/j.jnucmat.2012.03.009
17) J. Bischoff, A. T. Motta, C. Eichfeld, R. J. Comstock, G. Cao and T. R. Allen: *J. Nucl. Mater.*, **441** (2013), 604. https://doi.org/10.1016/j.jnucmat.2012.09.037
18) D. Gómez-Briceño, F. Blázquez and A. Sáez-Maderuelo: *J. Supercrit. Fluids*, **78** (2013), 103. https://doi.org/10.1016/j.supflu.2013.03.014
19) N.-q. Zhang, Z.-l. Zhu, H. Xu, X.-p. Mao and J. Li: *Corros. Sci.*, **103** (2016), 124. https://doi.org/10.1016/j.corsci.2015.10.017
20) Y. Behnamian, A. Mostafaei, A. Kohandehghan, B. Amirkhiz, R. Zahiri, W. Zheng, D. Guzonas, M. Chmielus, W. Chen and J. Luo: *J. Supercrit. Fluids*, **119** (2017), 245. https://doi.org/10.1016/j.supflu.2016.10.002
21) Y. Li, S. Wang, P. Sun, J. Yang, X. Tang, D. Xu, Y. Guo, J. Yang and D. D. Macdonald: *Corros. Sci.*, **135** (2018), 136. https://doi.org/10.1016/j.corsci.2018.02.036
22) T. Yang and P. Dou: *J. Iron Steel Res. Int.*, **32** (2025), 2609. https://doi.org/10.1007/s42243-025-01464-x
23) J. Zhou, L. Ren, Y. Lv, W. Lin, W. Jian, D. Zhang, X. Suo, D. Ruan and Q. Zhang: *J. Nucl. Mater.*, **605** (2025), 155566. https://doi.org/10.1016/j.jnucmat.2024.155566
24) F. Hou, S. Ding, Y. Wang, X. Kou and Y. Li: *J. Supercrit. Fluids*, **236** (2026), 107037. https://doi.org/10.1016/j.supflu.2026.107037
25) M. Wang, P. Yang, R. Li, B. Li, B. Ren, Y. Duan, M. Li and Y. Wang: *Appl. Surf. Sci.*, **749** (2026), 167989. https://doi.org/10.1016/j.apsusc.2026.167989
26) Y. Yi, Y. Watanabe, T. Kondo, H. Kimura and M. Sato: *J. Press. Vessel Technol.*, **123** (2001), 391. https://doi.org/10.1115/1.1373656
27) F. Froment, A. Tournié and P. Colomban: *J. Raman Spectrosc.*, **39** (2008), 560. https://doi.org/10.1002/jrs.1858
28) P. Colomban, S. Cherifi and G. Despert: *J. Raman Spectrosc.*, **39** (2008), 881. https://doi.org/10.1002/jrs.1927
29) K. F. McCarty and D. R. Boehme: *J. Solid State Chem.*, **79** (1989), 19. https://doi.org/10.1016/0022-4596(89)90245-4
30) Y. Matsuda, S. Hinotani and K. Yamanaka: *Tetsu-to-Hagané*, **79** (1993), 48. https://doi.org/10.2355/tetsutohagane1955.79.1_48

© 2026 ISIJ